Title

Characteristics of Mesoscale Convective Systems over China and Its Vicinity Using Geostationary Satellite FY2

Journal

Journal of Climate, 28(12)

ISSN

0894-8755

Authors

Yang, Xiangrong
Fei, Jianfang
Huang, Xiaogang
et al.

Publication Date

2015-06-15

DOI

10.1175/jcli-d-14-00491.1

Peer reviewed

Characteristics of Mesoscale Convective Systems over China and Its Vicinity Using Geostationary Satellite FY2

XIANGRONG YANG, JIANFANG FEI, XIAOGANG HUANG, AND XIAOPING CHENG

College of Meteorology and Oceanography, PLA University of Science and Technology, Nanjing, China

LEILA M. V. CARVALHO

Department of Geography, University of California, Santa Barbara, Santa Barbara, California

HONGRANG HE

College of Meteorology and Oceanography, PLA University of Science and Technology, Nanjing, China

(Manuscript received 8 July 2014, in final form 6 February 2015)

ABSTRACT

This study investigates mesoscale convective systems (MCSs) over China and its vicinity during the boreal warm season (May–August) from 2005 to 2012 based on data from the geostationary satellite Fengyun 2 (FY2) series. The authors classified and analyzed the quasi-circular and elongated MCSs on both large and small scales, including mesoscale convective complexes (MCCs), persistent elongated convective systems (PECSs), meso-β circular convective systems (MβCCSs), meso-β elongated convective system (MβECSs), and two additional types named small meso-β circular convective systems (SMβCCSs) and small meso-β elongated convective systems (SMβECSs). Results show that nearly 80% of the 8696 MCSs identified in this study fall into the elongated categories. Overall, MCSs occur mainly at three zonal bands with average latitudes around 20°, 30°, and 50°N. The frequency of MCSs occurrences is maximized at the zonal band around 20°N and decreases with increase in latitude. During the eight warm seasons, the period of peak systems occurrences is in July, followed decreasingly by June, August, and May. Meanwhile, from May to August three kinds of monthly variations are observed, which are clear northward migration, rapid increase, and persistent high frequency of MCS occurrences. Compared to MCSs in the United States, the four types of MCSs (MCCs, PECSs, MβCCSs, and MβECSs) are relatively smaller both in size and eccentricity but exhibit nearly equal life spans. Moreover, MCSs in both countries share similar positive correlations between their duration and maximum extent. Additionally, the diurnal cycles of MCSs in both countries are similar (local time) regarding the three stages of initiation, maturation, and termination.

1. Introduction

China and its vicinity, defined here as the area 18°–55°N, 70°–140°E, is a region highly influenced by a wide range of severe weather phenomena, such as frequent heavy precipitation, thunderstorms, gale winds, and hailstorms (Yu et al. 2007; Xie et al. 2010). All these severe weather phenomena cause safety problems for society and also damage agriculture, transportation, and communication systems (Wang and Cui 2011). Severe weather phenomena produced by frequent convective activity are often associated with mesoscale convective systems (MCSs). Although MCSs usually consist of regions with convective and stratiform precipitation and nonprecipitating regions with anvil cloud, a variety of precipitation and cloud structures can be exhibited (e.g., McAnelly and Cotton 1989; Johnson et al. 2005; Liu and Zipser 2013). MCSs may take on different organizations in regions with different environmental conditions (e.g., Carbone et al. 2002; Johnson et al. 2005; Houze 2004, 2007). As a result, in addition to having different scales (meso-α, meso-β, and meso-γ) as in Orlanski (1975), they may also appear with different morphologies, sometimes as a quasi-circular-shaped, long-lasting mesoscale convective complex (MCC; e.g., Maddox 1980),

Corresponding author address: Dr. Jianfang Fei, College of Meteorology and Oceanography, PLA University of Science and Technology, No. 60, Shuanglong Road, Nanjing 211101, China.
E-mail: feijf@sina.com

DOI: 10.1175/JCLI-D-14-00491.1

as a persistent elongated convective system (PECS; e.g., Anderson and Arritt 1998), or as a convective line (e.g., Houze 1977; Zipser 1977; Parker and Johnson 2000; Meng et al. 2013; Zheng et al. 2013; Liu and Zipser 2013).

MCSs can be organized in a variety of ways. Some evolve from discrete and somewhat isolated cells, whereas others occur within large complexes or lines. Many studies have shown that organization of the convection can be affected by the vertical wind shear, convective available potential energy (CAPE), and relative humidity, and by the vertical distributions of each of these variables (e.g., Moncrieff and Green 1972; Houze 1977, 2004; Rotunno et al. 1988; Laing and Fritsch 2000; Johnson et al. 2005; Meng et al. 2013; Zheng et al. 2013). For example, MCCs generally initiate within prominent baroclinic zones characterized by locally large values of lower-tropospheric vertical wind shear and CAPE (Laing and Fritsch 2000), while the meso-β-scale elongated systems tend to occur in more stable environments shown by a lower CAPE (Jirak et al. 2003). Particularly for convective lines, convection is usually aligned perpendicular (parallel) to the wind shear direction if there is significant vertical wind shear at low (middle) levels (Johnson et al. 2005; Zheng et al. 2013). These differences may affect the amount of stratiform and convective precipitation generated by a system, and consequently the vertical distribution of latent heat release (Houze 2004). Therefore, a detailed investigation of the morphology of convective regions in MCSs is important for understanding the relationship between MCSs and their environments.

Many studies of organized convection over China and its vicinity are based on observations from field campaigns, such as the South China Sea Monsoon Experiment (Lau et al. 2000), whereas some others are based on model simulations (Medina et al. 2010; Fei et al. 2011). The availability of multiple satellite observations in recent years provides an opportunity to describe in detail the properties and characteristics of MCSs (e.g., Houze 2007; Romatschke et al. 2010; Luo et al. 2011; Xu and Zipser 2011; Xu 2013; Liu and Zipser 2013; Wu et al. 2013; Qie et al. 2014). The findings are particularly helpful to understand the structures of MCSs and their relationships with the environments as they evolve. However, there are limitations in using satellite imagery to investigate MCSs. For instance, although the spatial resolution of polar orbiting satellites is satisfactory to investigate inner vertical structures of MCSs, the temporal resolution is inadequate to properly describe their life cycles. This is perhaps why geostationary satellites with their high temporal resolution data are commonly used to investigate MCSs. Many studies have conducted surveys on MCSs over China and its vicinity using geostationary satellite data, but the majority of these studies focused on a particular type of system known as a mesoscale convective complex (Li et al. 1989; Xiang and Jiang 1995; Yang and Tao 2005) or some special types of MCS, such as the MαCS and MβCS at meso-α and meso-β scales, respectively (e.g., Ma et al. 1997; Tao et al. 1998; Jiang and Fan 2002; Zheng et al. 2004, 2008). With exception of the studies by Zhuo et al. (2012) and Zeng et al. (2013) that examined MCS categories similar to those of Jirak et al. (2003) over central east China, few studies have focused on the morphology of convective regions in MCSs and respective relationships with large-scale environments.

The main goal of this study is to characterize the spatiotemporal distribution and properties of MCSs over China and its vicinity separated according to their morphologies. For this purpose, we examine eight years of observations from the geostationary satellite Fengyun 2 (FY2) series. With the samples derived from FY2 observations, the morphological characteristics of MCSs are analyzed with varied statistical approaches.

This paper is organized as follows. Datasets and methodology are described in section 2. The analysis of characteristics for all MCS types and the comparison of MCSs features between China and North America are presented in section 3. Finally, section 4 gives a summary of this study and discusses some of its implications.

2. Data and methodology

a. Input data

The data used in this study are digital IR images of FY2 series geostationary meteorological satellites C and E (*FY-2C* and *FY-2E*), provided by the National Satellite Meteorological Center of the China Meteorological Administration (CMA; http://nsmc.cma.gov.cn/NewSite/NSMC_EN/Home/Index.html). The *FY-2C* was launched on 19 October 2004, and the *FY-2E*, which extends service for *FY-2C*, was launched on 23 December 2008. The products of both the *FY-2C* and *FY-2E*, with a 0.1° × 0.1° spatial resolution over the domain of 60°S–60°N, 45°–165°E, are provided once an hour. Since most convective systems occur in the warm season, this study focuses on imagery data from May to August. However, since the *FY-2E* products are available only after the winter of 2009, we use *FY-2C* data during 2005–09 and *FY-2E* data during 2010–12. Figure 1 shows the annual and monthly integral ratio of satellite data, which is calculated by the times of data available to the whole times during a specific time series. It indicates that the average integral ratio is 96%, and that *FY-2E* has a better integral ratio than *FY-2C*. Meanwhile, the operational

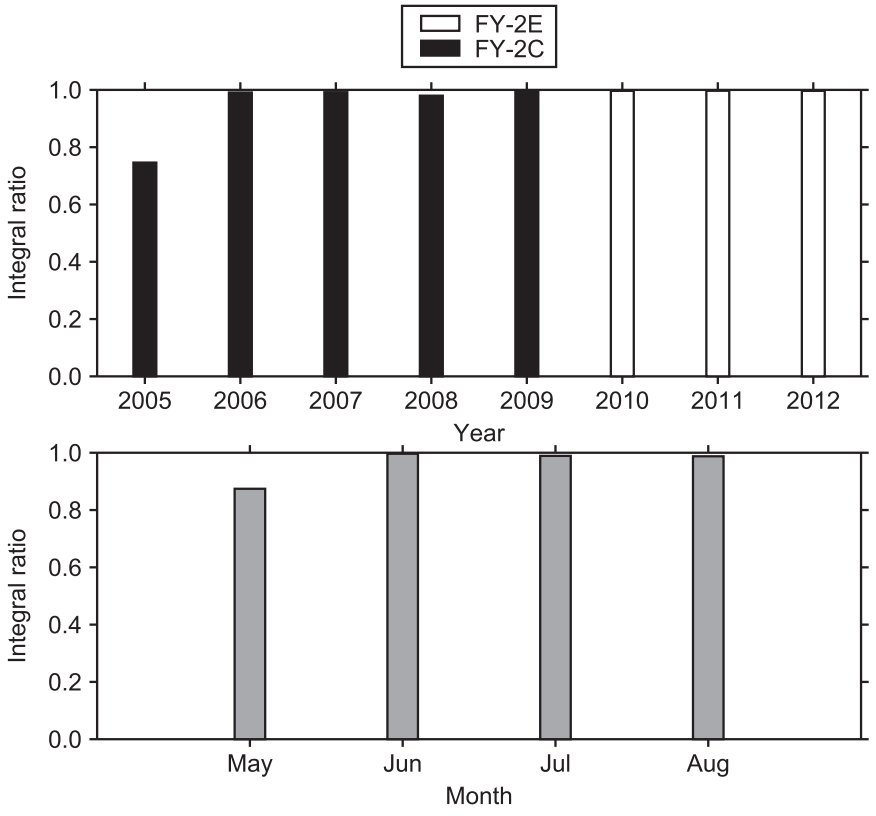

FIG. 1. Integral ratio of FY2 series geostationary satellite data: (top) annual and (bottom) monthly ratio. The integral ratio is calculated as the ratio of the time that data were available to the whole time period during a specific time series.

objective weather-map analysis made at the National Meteorological Center of the CMA is also used to help determine the presence of cold waves. The maps of weather analysis on the ground surface are available four times per day (0000, 0600, 1200, and 1800 UTC), and those on the isobaric surfaces (850, 700, and 500 hPa) are available twice per day (at 0000 and 1200 UTC). In addition, the best-track dataset provided by the Japan Meteorological Agency is also utilized.

b. *Satellite classification of MCSs*

A milestone of MCS survey using geostationary satellite imageries is the work by Maddox (1980). This study investigated quasi-circular meso-α-scale convective systems that frequently move across the central United States. The author defined these systems with similar shape, area, and duration on infrared satellite imageries as a particular type of MCS, which was termed a mesoscale convective complex (MCC; Table 1 in Maddox 1980). After that, a large number of studies on MCCs have been conducted worldwide (Rodgers et al. 1983, 1985; Velasco and Fritsch 1987; Augustine and Howard 1988, 1991; Cotton et al. 1989; Miller and Fritsch 1991; Laing and Fritsch 1997). To simplify the identification and documentation process, Augustine and Howard (1988) removed the size requirement that areas with brightness temperature $\leq -32°C$ must be no less than 100 000 km^2 in Maddox (1980). They considered that the $-52°C$ threshold can adequately represent the evolution of the storm (Kane et al. 1987; Augustine and Howard 1988). This modified MCC definition has been adopted by many other studies on MCCs (Augustine and Howard 1991; Jirak et al. 2003; Durkee and Mote 2010; Blamey and Reason 2012). The present study also uses the modified MCC definition to examine the MCCs (Table 1). Meanwhile, based on the findings from Bartels et al. (1984) that MCCs only account for part of the MCSs, Anderson and Arritt (1998) identified another large class of MCSs that they classified as persistent elongated convective systems (PECSs). This type of MCS, which differentiates from the MCC only with regard to the shape of the system (Table 1), accounts for approximately 70% of MCSs and plays an important role in producing severe weather phenomena over the United States (Anderson and Arritt 1998). Based on these definitions, Jirak et al. (2003) classified four types of MCSs.

TABLE 1. MCS definitions based on the analysis of IR satellite imagery. Note that there are two additional types of MCSs other than the definitions by Jirak et al. (2003).

MCS category	Size	Duration	Shape
MCC	Cold cloud region $\leq -52°C$ with an area $\geq 50\,000\ km^2$	Size definition met for ≥ 6 h	Eccentricity ≥ 0.7 at time of maximum extent
PECS			$0.2 \leq$ eccentricity < 0.7 at time of maximum extent
MβCCS	Cold cloud region $\leq -52°C$ with an area $\geq 30\,000\ km^2$ and maximum size must be $\geq 50\,000\ km^2$	Size definition met for ≥ 3 h	Eccentricity ≥ 0.7 at time of maximum extent
MβECS			$0.2 \leq$ eccentricity < 0.7 at time of maximum extent
SMβCCS	Cold cloud region $\leq -52°C$ with an area $\geq 30\,000\ km^2$ and maximum size $< 50\,000\ km^2$		Eccentricity ≥ 0.7 at time of maximum extent
SMβECS			$0.2 \leq$ eccentricity < 0.7 at time of maximum extent

The other two types of MCSs are the meso-β circular convective system (MβCCS) and meso-β elongated convective system (MβECS), which are relatively small MCC and PECS, respectively. The definitions of these four MCS types are listed in Table 1.

China and North America extend across similar range of latitudes in the Northern Hemisphere. Thus, with the additional purpose of comparing MCS characteristics between China and North America, four MCS types (MCCs, PECSs, MβCCSs, and MβECSs) are investigated in this study using the definitions provided by Jirak et al. (2003). Furthermore, two additional types of MCSs, small meso-β circular convective system (SMβCCS) and small meso-β elongated convective system (SMβECS), are examined here due to the relatively large number of these systems over central east China (Zeng et al. 2013). These two categories of systems are defined with similar criteria as the corresponding types MβCCS and MβECS, except that the cloud shield with IR brightness temperature $\leq -52°C$ needs to be less than $50\,000\ km^2$ at the maturation stage of the system. A detailed description of all MCS categories surveyed in this study is provided in Table 1. In addition, three key stages—initiation, maturation, and termination—are defined during the MCS life cycle. Initiation is the period when size criterion is first satisfied; maturation is the period when contiguous cold-cloud shield (IR temperature is $-52°C$) reaches maximum size; termination is the period when the size criterion is no longer satisfied.

c. *Formation method of MCS datasets*

The most common methods to investigate MCSs using infrared satellite imageries can be divided into three categories: manual, half-automated, and automated. The manual method consists of visually inspecting satellite images and then subjectively identifying systems (Maddox 1980; Maddox et al. 1982; Miller and Fritsch 1991; García-Herrera et al. 2005a; Zhuo et al. 2012). The automated method objectively classifies the systems within images (Augustine and Howard 1988, 1991; Machado et al. 1998; Carvalho and Jones 2001; Morel and Senesi 2002; Jirak et al. 2003; Zheng et al. 2004, 2008; García-Herrera et al. 2005b; Li et al. 2012). The half-automated method, also named the hybrid approach, usually consists of two steps: the automated identification of convective clouds followed by a subjective tracking of these systems (e.g., Durkee and Mote 2010) or automated classification of the systems followed by a visual check to verify their evolution (e.g., Blamey and Reason 2012). The automated method is undoubtedly the most efficient and objective way to classify MCSs using a long series of satellite images. However, there are important caveats in the automated methods. Among the most common problems is the identification of splitting and merging of MCSs as they evolve (Machado et al. 1998; Carvalho and Jones 2001; Durkee and Mote 2010). Thus, in this study we propose to use a half-automated approach similar to Blamey and Reason (2012), in which systems are identified and tracked through an automated method subsequently followed by a visual inspection.

The automated method adopted in this study is the "maximum spatial correlation tracking technique" (MASCOTTE) developed by Carvalho and Jones (2001). This tracking method was originally developed to select and identify cloud features based on infrared brightness temperature below a predetermined temperature threshold and cloud area above a given size. Systems are then tracked based on the maximum spatial correlation between the target system and all other systems in a consecutive image. Once a system is identified, the method calculates several properties of the cloud features such as mean and minimum cloud shield temperatures, area of the MCS and of the coldest cluster, number of cold clusters

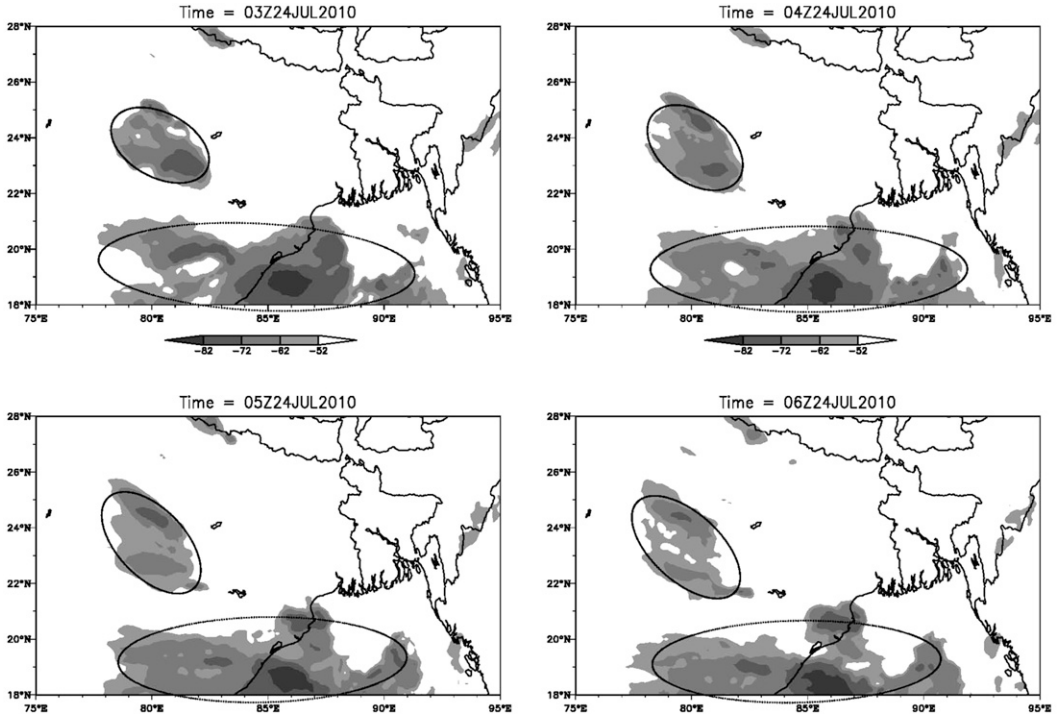

FIG. 2. The two identified MCSs in consecutive images at 0300–0600 UTC 24 Jul 2010. The shaded area is the area with IR brightness temperature $<-52°C$. The system at the boundary of the domain is considered as the boundary system and excluded from the MCS datasets.

embedded in the cloud systems, eccentricity, displacement, and duration of the MCS, and provides indications about merging and splitting of the systems. MASCOTTE was used to track MCS systems over South America (Carvalho and Jones 2001), Spain (García-Herrera et al. 2005b), and southern Africa (Blamey and Reason 2012).

The hybrid method used in this study is performed as follows. First, the identification and temporal evolution of MCS are conducted using MASCOTTE [see Carvalho and Jones (2001) for details]. The method produces two outputs for each image investigated during the tracking at a given time t. One output records the unique identification and physical properties of all MCSs at that time. The other is an image that includes cloud shields that meet the MCS criteria and their respective fitting ellipses outlines (Fig. 2). Based on these two outputs, the second step consists of a visual verification of the evolution of MCSs to identify situations that may lead the automatic tracking to search for wrong targets. The most common of these conditions is the occurrence of merging and/or splitting, as well as missing images. If the automatic tracking misinterprets the real temporal evolution of the MCS due to merging or splitting of systems, we adopt the Durkee and Mote (2010) approach. That is, when a system splits, the cloud shield that closely resembles the previous scene is assigned as a continuation of the life cycle of that system. The closely resembled system is often the largest cloud shield within the split or the nearest cloud shield judged by a sequence of consecutive images. When a system is observed to merge with another, the merged system is considered as a continuation of the life cycle of the larger system. The method considers that the life cycle of the relatively small system terminates at the time of the merging. In the case of missing images, the continuation of any MCS life cycle is decided based on the images that are available. If the missing interval exceeds 3 h, the MCSs whose life cycles are incomplete due to insufficient temporal resolution are excluded from the datasets and they are called ''missing MCSs'' (M-MCS; Table 2).

Finally, it is worth noting that other systems such as cold waves in the pre-summer season and typhoons in the warm season may also meet the satellite-based MCS criteria listed in Table 1. Thus, a further check is performed to exclude two types of common systems: cold waves, which can be identified from weather maps, and typhoons that are recorded by the best-track dataset provided by the Japan Meteorological Agency. Other systems also excluded from the dataset are boundary systems (BDS; Table 2) whose cloud shields intercept the boundaries of the studied domain as their

TABLE 2. MCS types and numbers observed from May to August during 2005–12.

Type	MCC	PECS	MβCCS	MβECS	SMβCCS	SMβECS	BDS	M-MCS
Number	610	2467	734	3099	426	1360	227	3

properties could be incorrectly assessed by the tracking technique (Fig. 2).

3. Results

a. Spatial distribution

During the eight warm seasons from 2005 to 2012, 8696 MCSs over China and its vicinity are identified and classified (see Table 2). Among all MCSs, 1770 systems are categorized as quasi-circular MCSs (MCCs, MβCCSs, and SMβCCSs) and the rest as elongated MCSs (PECSs, MβECSs, and SMβECSs), indicating that elongated systems account for nearly 80% of the MCSs during the studied period. Moreover, more systems belong to small-scale MCS categories (MβCCSs, MβECSs, SMβCCSs, and SMβECSs) compared to large ones (MCCs and PECSs). There are 5619 systems classified as small-scale convective systems, and only 3077 as large-scale convective systems. Thus, the dominant systems in this study are the small-scale and elongated MCSs. This finding is basically consistent with the results observed over central east China (e.g., Zeng et al. 2013) but different from what has been previously classified over the lower reaches of the Yellow River in China (e.g., Zhuo et al. 2012) and central United States (e.g., Jirak et al. 2003).

Figure 3a shows the initiation locations of all MCSs during the 8-yr period. There are three preferred zonal bands for the initiations of MCSs: around 20°, 30°, and 50°N. The maximum frequency of initiation location is observed around 20°N and then decreases with latitude. Furthermore, there are several high-frequency centers in each zonal band. The first band is located mainly at low latitudes and is affected by the South Asia summer monsoon and intertropical convergence zone (ITCZ) during the boreal summer (e.g., Waliser and Gautier 1993; Ding and Chan 2005; Houze 2007; Romatschke et al. 2010). The high-frequency centers in this band include the western North Pacific region east of the Philippines, the southern China coastal region, southern China, the northern Indo-China, the Bay of Bengal, and regions south of the Himalayas (e.g., eastern India and Bangladesh) (Fig. 3c). The second band of MCS preferred initiation locations seems to be associated with topographic features and extends from the Tibetan Plateau in the west to the maritime region east of China. This band is influenced by the summer monsoon, which affects the topographically induced rainbands in the Tibetan Plateau, and the combination of East Asian summer monsoon and mei-yu front, which extends from the eastern plateau to the ocean (e.g., Ding and Chan 2005; Xu and Zipser 2011; Xu 2013). Several centers with relatively high frequencies are observed as well. From west to east, these centers are located over the central eastern Tibetan Plateau, the western Sichuan Plateau and Hengduan Mountains east of the Tibetan Plateau, eastern China, and the oceanic area around the Ryukyu Islands (Fig. 3c). The third and northernmost latitudinal band, which is also the band with the lowest MCS activity, is observed around 50°N. A high frequency of MCS activity in this band is observed in the southwest region of the Lake Baikal (Fig. 3c). The MCS occurrences in this band are generally related to low-level troughs and are accompanied by significant lightning activity as observed by satellite (Zheng et al. 2008).

The clustering of MCSs along the three zonal bands and high-frequency centers are also apparent in Fig. 3b, which shows the frequency of MCS locations throughout their life cycles. Notice that the region with the highest frequency observed over the northern Indo-China (Fig. 3a) shifts toward the Bay of Bengal in Fig. 3b. A possible reason for this shift is a longer average duration of MCSs near the Bay of Bengal compared to the northern Indo-China. Overall, the characteristics of MCS spatial distribution are similar to the results derived from an investigation of frequency of −52°C IR temperature at each grid over East Asia in Zheng et al. (2008), excluding the high-frequency center over the western North Pacific shown in that work. This difference can be explained by a large number of typhoons with active spiral rainbands that occur over the western North Pacific (e.g., Ha et al. 2013, 2014; Ma et al. 2015) and eventual boundary systems near the bottom boundary of the domain, all excluded in this study.

Figure 4 shows the spatial distribution of the initiation locations for the six MCS types investigated in this study. Although the high-frequency centers of the six MCS types shown in Fig. 4 are similar to that in Fig. 3a, different MCS categories tend to cluster in their own preferred locations. For example, the quasi-circular MCSs occur mainly at the two low-latitude bands influenced by the boreal summer monsoon and the ITCZ (Figs. 4a,c,e). High-frequency centers of these quasi-circular MCSs are located predominantly over

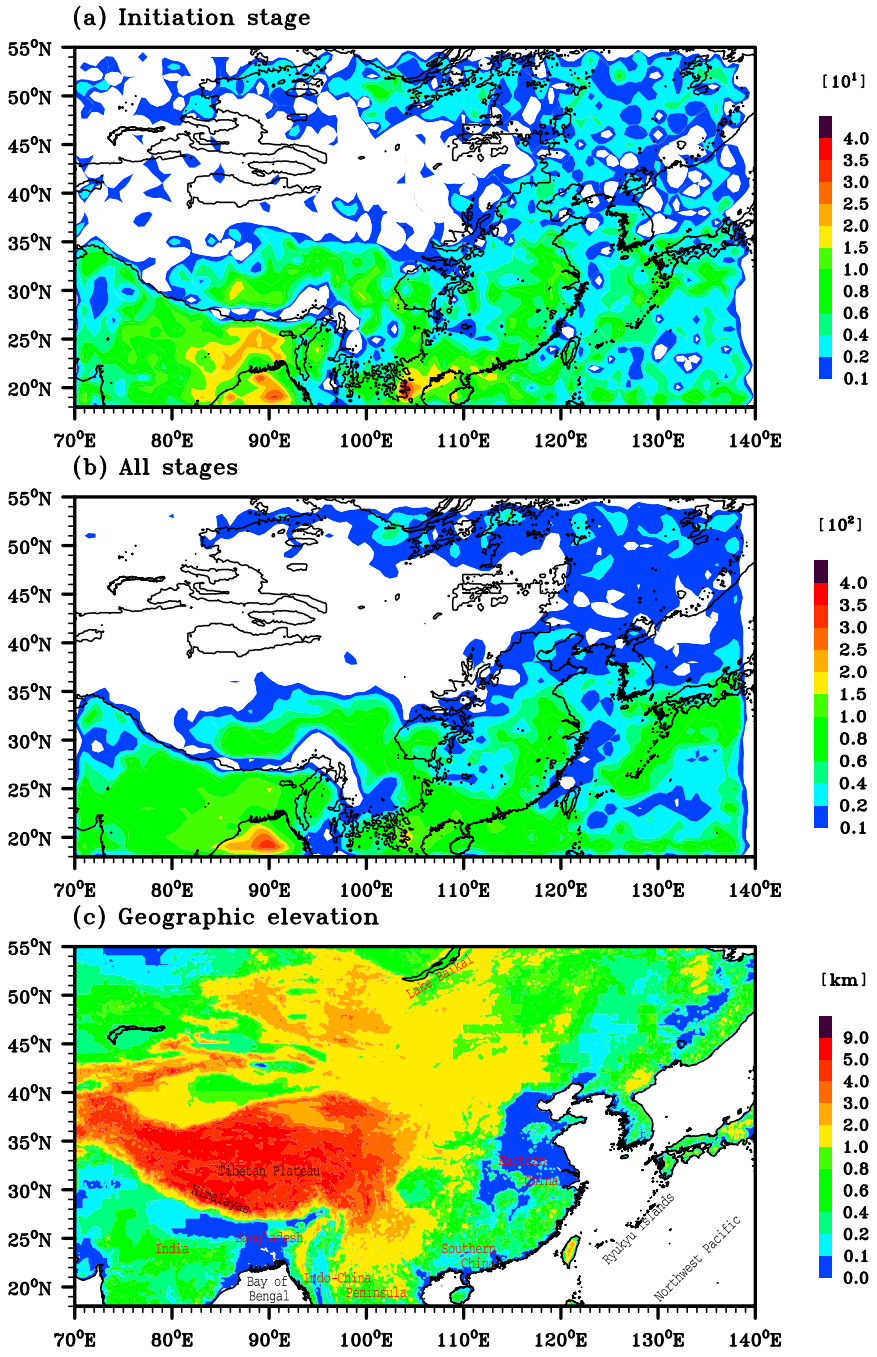

FIG. 3. Locations of MCSs and geographic elevations over China and its vicinity: (a) initiation stage, (b) all stages of the MCS evolution, and (c) geographic elevations. Note that (a) and (b) are created by clustering the MCS origins into 1° grid box; the color shading shows the frequency of MCS occurring in each grid box.

the Bay of Bengal, northern Indo-China, and regions south of the Himalayas. More specifically, the highest frequency of initiation locations of both MCCs and MβCCSs are observed over the Bay of Bengal, while the initiation locations of SMβCCSs are more frequent over the northern Indo-China. Unlike the quasi-circular systems, the elongated systems account for the majority of the total MCSs and distribute almost in all the three zonal bands (Figs. 4b,d,f). Regarding PECSs and MβECSs, the highest frequency centers of their

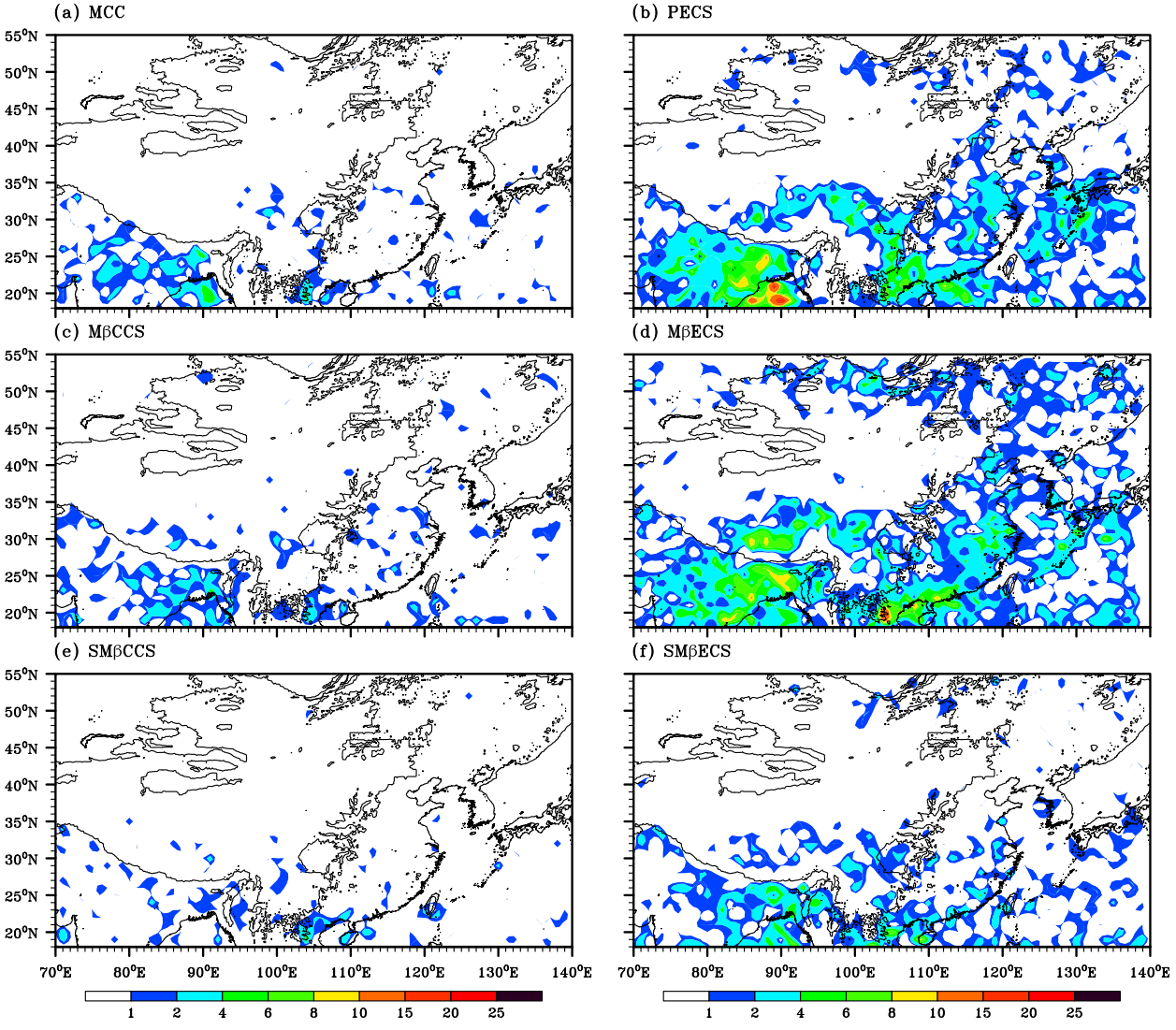

FIG. 4. As in Fig. 3a, but for six types of MCSs: (a) MCC, (b) PECS, (c) MβCCS, (d) MβECS, (e) SMβCCS, and (f) SMβECS.

initiations are observed over the Bay of Bengal and northern Indo-China, respectively, whereas SMβECSs exhibit nearly equal probability over both regions. Besides, regions over the Bay of Bengal and south of the Himalayas, where both MCCs and PECSs are more frequent, are also the regions where meso-α-scale systems dominate (Figs. 4a,b). On the other hand, meso-β-scale systems are predominant over the Tibetan Plateau and the northernmost band around 50°N. Few MCCs are observed over the Tibetan Plateau in our records and the dominant type of MCS in this region is MβECS (Figs. 4a, d). These relatively small-scale systems observed over the Tibetan Plateau are likely associated with the steep topography and orographic lifting leading to rapid MCS formation and further splitting (Jiang and Fan 2002; Yang and Tao 2005), resulting in small-scale MCSs.

b. *Interannual and monthly variability*

Over the eight warm seasons, we observe a considerable interannual variability in the occurrence of MCSs in the studied domain, with an average of about 1087 systems and a range between minimum 893 and maximum 1484 MCSs per season (Fig. 5). The peak of MCS occurrences happens in 2010, followed by 2008 with a total of 1191. Regarding the monthly variability, the peak in MCS occurrences is observed during July, followed decreasingly by June, August, and May.

In addition to the monthly variability of the total MCSs, there is an obvious modification in their spatial distributions. Figure 6 shows the spatial distribution of MCS initiation locations from May to August. We can identify three main types of monthly variations:

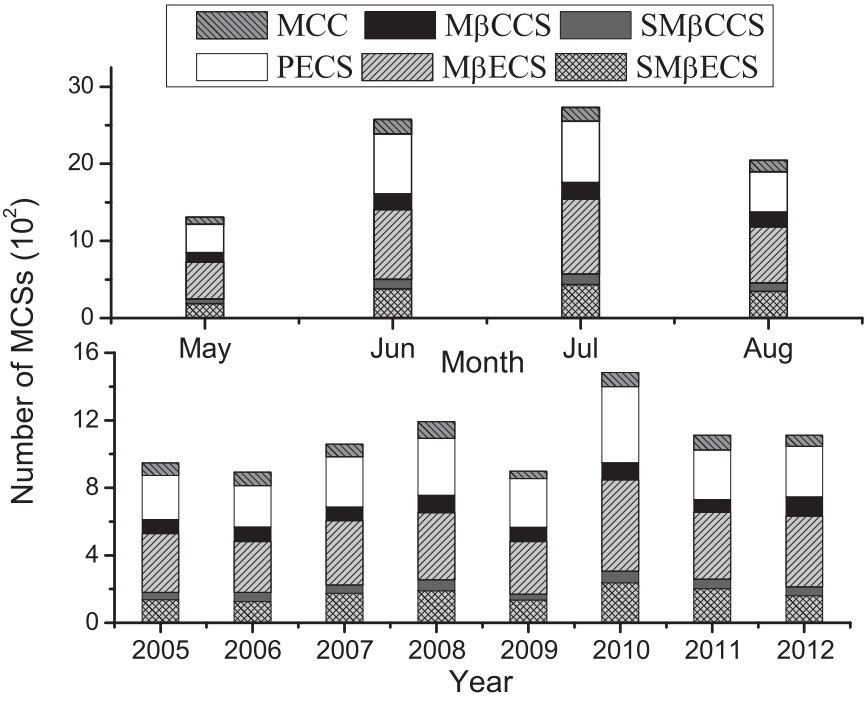

FIG. 5. Distribution of (top) monthly and (bottom) annual MCSs.

northward migration, rapid increase in the number of systems, and persistent high frequency of MCS occurrences. The first type is the northward migration. The peaks in the frequency of MCSs over south China, the northwestern Yun-Gui Plateau, the south part of eastern China, and the Ryukyu Islands occur in June, and then the high-frequency centers move to the north part of eastern China and regions around the Kyushu Island in July, and keep their northernmost centers until August (Figs. 6b–d). The main reasons for this northward migration are the East Asian summer monsoon (EASM) and subtropical high (Ding and Chan 2005; Xu and Zipser 2011). After the onset of the monsoon, southerly and southwesterly flow from both systems carry warm and moist tropical air from the equatorial regions to the north, leading to a more favorable environment for the occurrence of MCSs. As the EASM and the subtropical high move northward during midsummer, favorable regions for the development of MCSs also move in phase, which explains the observed high-frequency centers of MCS occurrences (Fig. 6c). The second type, which is a rapid increase in the number of MCS activity during the warm season, is observed over the Tibetan Plateau and the area east of it. Notice that nearly no MCS occurs over the Tibetan Plateau in May (Fig. 6a), and only a few occur in June (Fig. 6b). However, a rapid increase of MCS activity occurs in July (Fig. 6c) and a considerable decrease in the total number of systems is followed in August (Fig. 6d). Romatschke et al. (2010) and Qie et al. (2014) investigated the increase of extreme convection over the Tibetan Plateau during the monsoon season and indicated that the westerly winds and high relative humidity are likely related to the formation of systems in this region. During the monsoon season, westerly winds weaken gradually from May to August, and relative humidity increases westward from the eastern Tibetan Plateau. Then the strong heating over the Tibetan Plateau leads to shallow surface depression and a deep high in the middle and upper troposphere, ultimately intensifying upward motions induced by the Tibetan Plateau, particularly between June and July. Thus a combination of orographically induced upward motion and an increase of water vapor content in the atmosphere could explain the increase in the frequency of MCSs. The decrease in August is likely related to variations in the monsoonal circulation during the summer season. However, further studies are necessary to properly identify these mechanisms. The third type of monthly variation is the persistent high frequency of MCS occurrence, which means that there are regions where the MCS occurrences are persistently active during the warm seasons compared to the others. Those regions include the Bay of Bengal, regions south of the Himalayas, and the northern Indo-China (Houze 2007; Romatschke et al. 2010; Xu and Zipser 2011; Qie et al. 2014).

Figure 7 illustrates the monthly variability of the six MCS types. Interestingly, the occurrences of elongated systems exhibit a more pronounced monthly variability

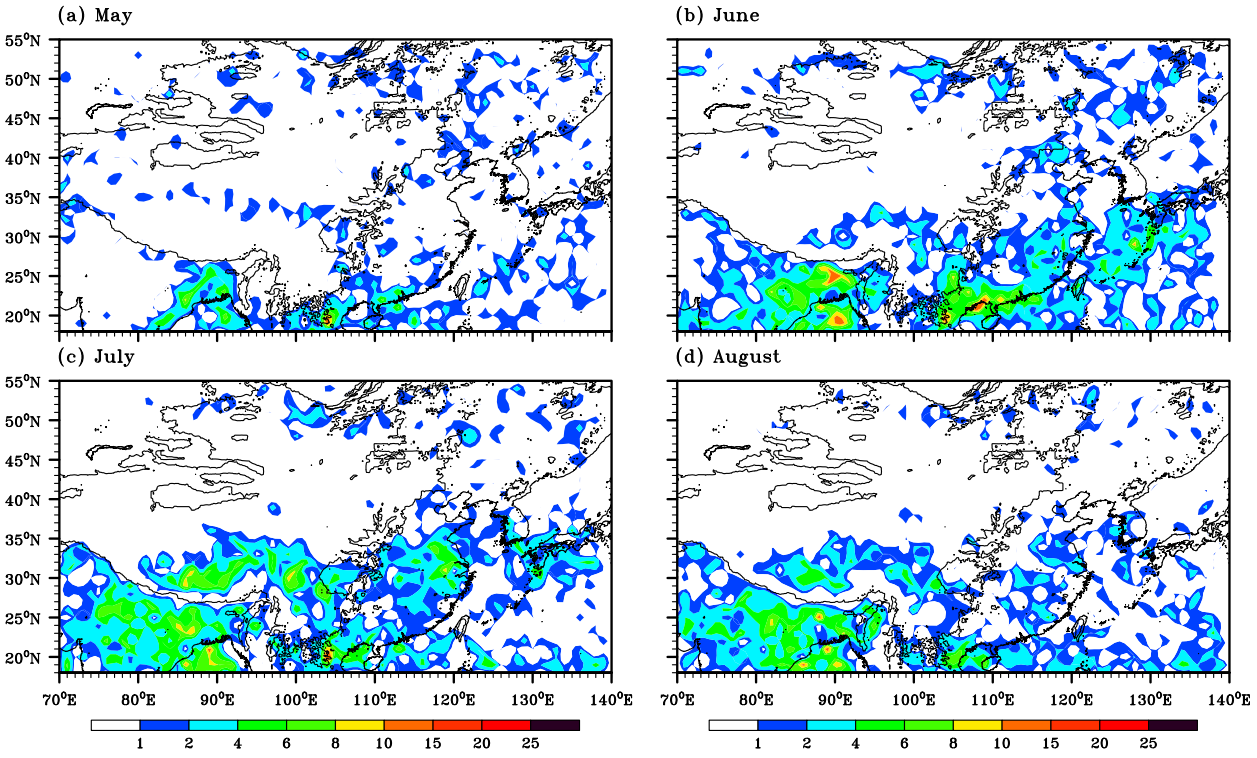

FIG. 6. As in Fig. 3a, but for the monthly spatial distribution of MCS origin locations from May to August: (a) May, (b) June, (c) July, and (d) August.

when compared to the quasi-circular systems. The frequency of elongated MCSs increases from May to July and then decreases in August, while quasi-circular systems show no obvious monthly differences except for the minimum occurrence of systems in May (Figs. 7a–c).

c. *Evolution characteristics*

Figure 8 displays the diurnal cycles of MCS occurrences for three key stages of MCS life cycles: initiation, maturation, and termination. MCSs can initiate, reach maximum extent, and decay at any time of the day, but an obvious diurnal cycle is shown for each stage. A high frequency of MCS initiation occurs during late afternoon to early evening hours in local standard time (LST = UTC + 7 h) and persists for about 6 h, predominantly between 1400 and 2000 LST. More specifically, MCS initiation begins to increase around 1400 LST and keeps increasing for the next 3 h, reaching the highest frequency around 1700 LST. In the following three hours, we observe a gradual decrease in the frequency of MCS initiation. The diurnal cycles of maturation, termination, and initiation share some similar characteristics. That is, the high frequencies of maturation and termination stages also persist nearly 6 h, with the peak frequencies observed mainly between 1600 and 2200 LST and between 1800 and 0000 LST, respectively (Fig. 8). Moreover, both stages show a gradual increase in the first three hours of the six high-frequency hours and then gradually decrease in the following three. Thus, the times for the highest frequency of initiation, maturation, and termination are 1700, 1900, and 2100 LST, respectively, implying that the period with the peak frequency of MCS maturation (termination) occurs just 2 h after the initiation (maturation). However, there is a small difference in the number of MCSs at the peak frequency of each key stage. That is, the number of MCSs in the initiation (maturation) stage is greater than the number of MCSs in the maturation (termination) phase, showing that MCSs are more concentrated in the initiation stage than the other two stages at that period. In addition, notice that there is a secondary peak for each stage, at 0200, 0500, and 0700 LST for MCS initiation, maximum extent, and termination, respectively.

Although different MCS types show similar diurnal cycles in the frequency of their three stages, there are unique characteristics for some types, especially the quasi-circular systems (Fig. 9). For example, MCC initiation peaks on average between 1500 and 1800 LST, and maturation between 1800 and 2100 LST, about 3 h after the initiation. The termination of MCC occurs predominantly between 2100 and 0100 LST, which is almost 4 h later from the peak frequency of maturation

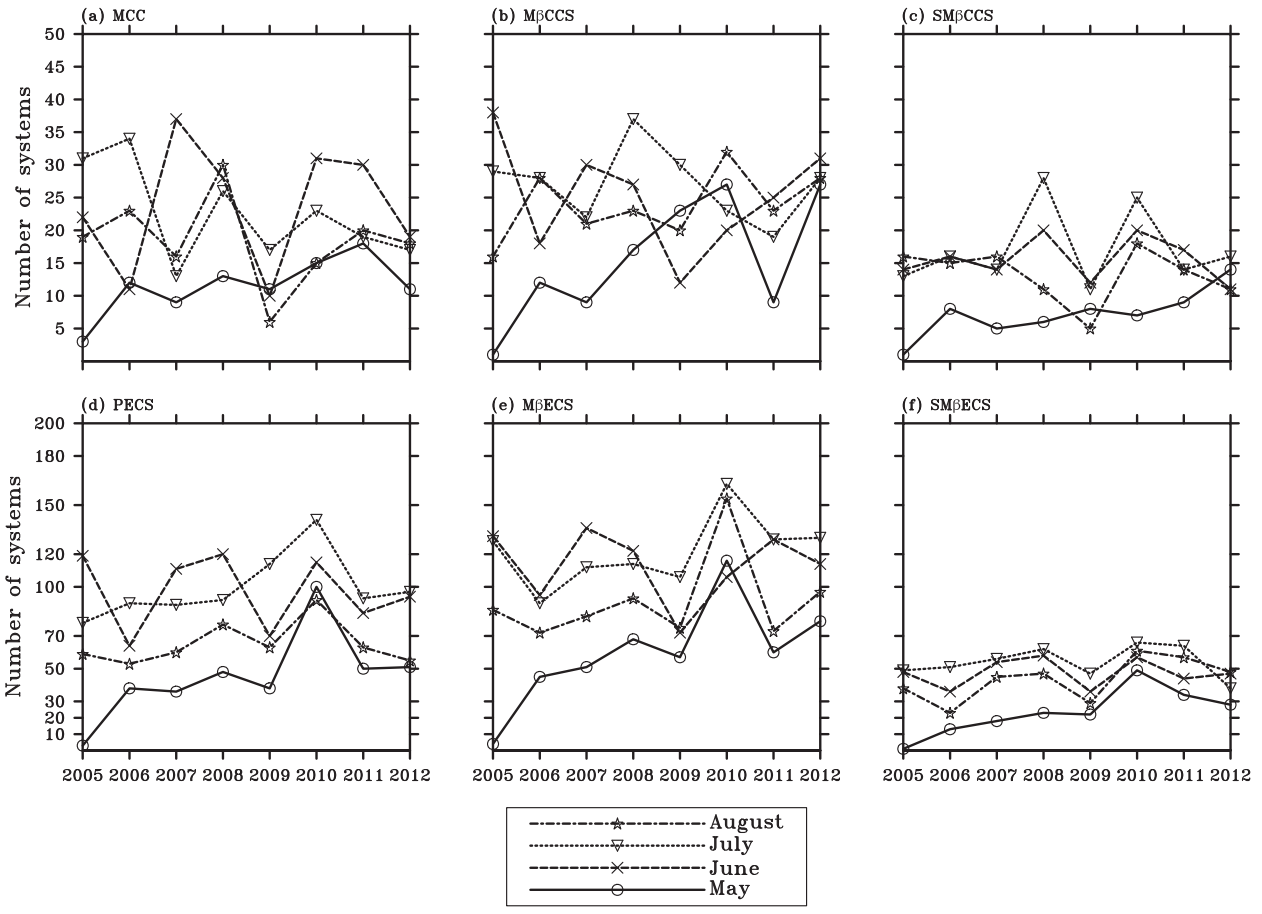

FIG. 7. The monthly totals of all MCS types over the eight warm seasons in each month: (a) MCC, (b) MβCCS, (c) SMβCCS, (d) PECS, (e) MβECS, and (f) SMβECS.

stage. Meanwhile, MCCs exhibit a secondary peak in the frequency of initiation and maturation stages at 0100 and 0400 LST, respectively (Fig. 9a). These secondary peaks are both an hour earlier than the two maxima observed for the total MCSs around 0200 and 0500 LST, respectively (Fig. 8). Regarding MβCCSs, although the high frequencies of the maturation and termination stages occur during 1700–2200 LST and 1900–0000 LST, respectively, both stages peak at 2100 LST (Fig. 9c). As for SMβCCSs, the temporal overlap in the high frequencies of the three stages is more obvious than for the other two quasi-circular systems. The peak frequency of maturation (termination) is only one hour later than the peak of initiation (maturation) (Fig. 9e). Compared to the quasi-circular systems, the elongated MCSs share more similar diurnal cycles to the total MCSs, which are more concentrated in the afternoon peak for each key stage. For instance, about half of the MβECSs show high frequencies of the key stages during the time windows 1400–2000, 1600–2200, and 1800–0000 LST, respectively (Fig. 9d).

In summary, MCSs over China and its vicinity generally initiate in the afternoon, mature from dusk to midnight, and dissipate during late night to early morning hours in LST. This diurnal cycle, which is mainly affected by the diurnal variation of solar radiation, has also been documented in previous works over China (Zheng et al. 2008; Xu and Zipser 2011; Li et al. 2012) and some other regions worldwide (e.g., Carvalho et al. 2002; Jirak et al. 2003; Nesbitt and Zipser 2003; Durkee and Mote 2010; Romatschke et al. 2010; Blamey and Reason 2012). The secondary peaks in frequency of MCSs in the three stages are likely due to environments that favor nocturnal convection. For instance, Romatschke et al. (2010) indicated that the wide convective cores over land show a midnight-to-early morning maximum along the Himalayan foothills, which is associated with convergence of moist southwesterly monsoonal air with the diurnally cooled downslope flow. Xu and Zipser (2011) showed that nocturnal maximum precipitation features occur in the foothills of the southeastern Tibetan Plateau, which results from a nocturnal low-level inflow of moist air that

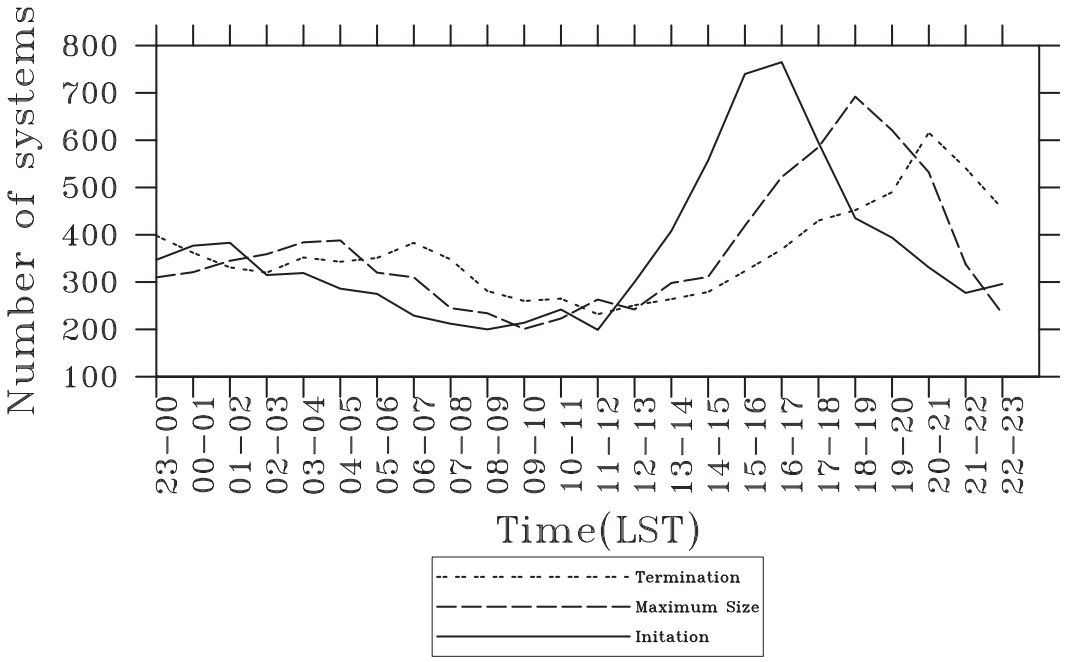

FIG. 8. Frequency for all MCSs during MCS initiation, maturation, and termination stages.

may assist the formation and maintenance of the nocturnal occurrence appearing over the foothills of the Himalayas in the evening. In addition, there are also nocturnal MCSs occurring in oceanic regions and over northeastern China.

The average duration of the 8696 MCSs over the studied domain is 7.35 h (Table 3), which is slightly longer than that over central east China (~6.6 h; Zeng et al. 2013), but much shorter than the duration found over the lower reaches of Yellow River (10.0 h; Zhuo et al. 2012). Figure 10 shows the 3-h bin distribution of MCS durations. It illustrates that the number of total MCSs decreases with duration, and so do the α-scale or β-scale systems. Over 70% of the MCSs have their life spans between 3 and 9 h, and the systems peak in the first 3-h bin from the necessity duration per definition on a α scale (6 h) or β scale (3 h). More specifically, SMβCCSs and SMβECSs maximize in duration between 3 and 6 h, and fewer systems exhibit duration between 6 and 9 h. The longest life cycle for these two systems is 12 h, and few of them last between 9 and 12 h. The number of MβCCSs and MβECSs with durations between 3 and 6 h is nearly the same as between 6 and 9 h. Then a pronounced decrease in the number is observed for the intervals between 9 and 12 h, and the number of systems with life span around 18 h is virtually zero. Similar to the β-scale systems, MCCs and PECSs peak between 6 and 9 h, following by a large decrease between 9 and 12 h, and then a gradual decrease for the following 3-h bins. In addition, PECSs and MCCs account for the majority of systems with duration longer than 9 h, and some of them even last longer than 24 h (Fig. 10). Furthermore, Table 3 indicates that the average duration of an MCS's developing stage (4.27 h) is slightly longer than the respective decay stage (4.03 h), indicating that the decaying stage is faster than the development stage of MCSs.

Figure 11 shows the size distribution of the MCS maturation stage. Excluding the two classes with areas from 30 000 to 50 000 km^2 (SMβCCSs and SMβECSs), this figure indicates a negative exponential relationship between the number of MCSs and their area (e.g., Jirak et al. 2003). It shows that the largest number of MCSs reaches maximum size of about 50 000–80 000 km^2, and these systems are predominantly MβCCSs and MβECSs. However, the ratio of α-scale systems to β-scale systems gradually increases from the area bin between 80 000 and 110 000 km^2. The number of MCCs and PECSs largely increases in the interval 80 000–140 000 km^2, whereas the number of MβCCSs and MβECSs decreases. From the average maximum size exceeding 140 000 km^2, all MCSs types decrease with size and only a few β-scale systems exist. Moreover, the maximum size of the β-scale systems is roughly 230 000 km^2, while some of the PECSs and MCCs have a maximum extent larger than 350 000 km^2 (Fig. 11). The detailed analysis of the average maximum size of each MCS type is shown in Table 3. It shows that the average size of the 8696 MCSs is 105 300 km^2, about 10% larger than that reported by Zeng et al. (2013). In addition, PECSs have the largest average maximum area (larger than 180 000 km^2) and the average maximum area

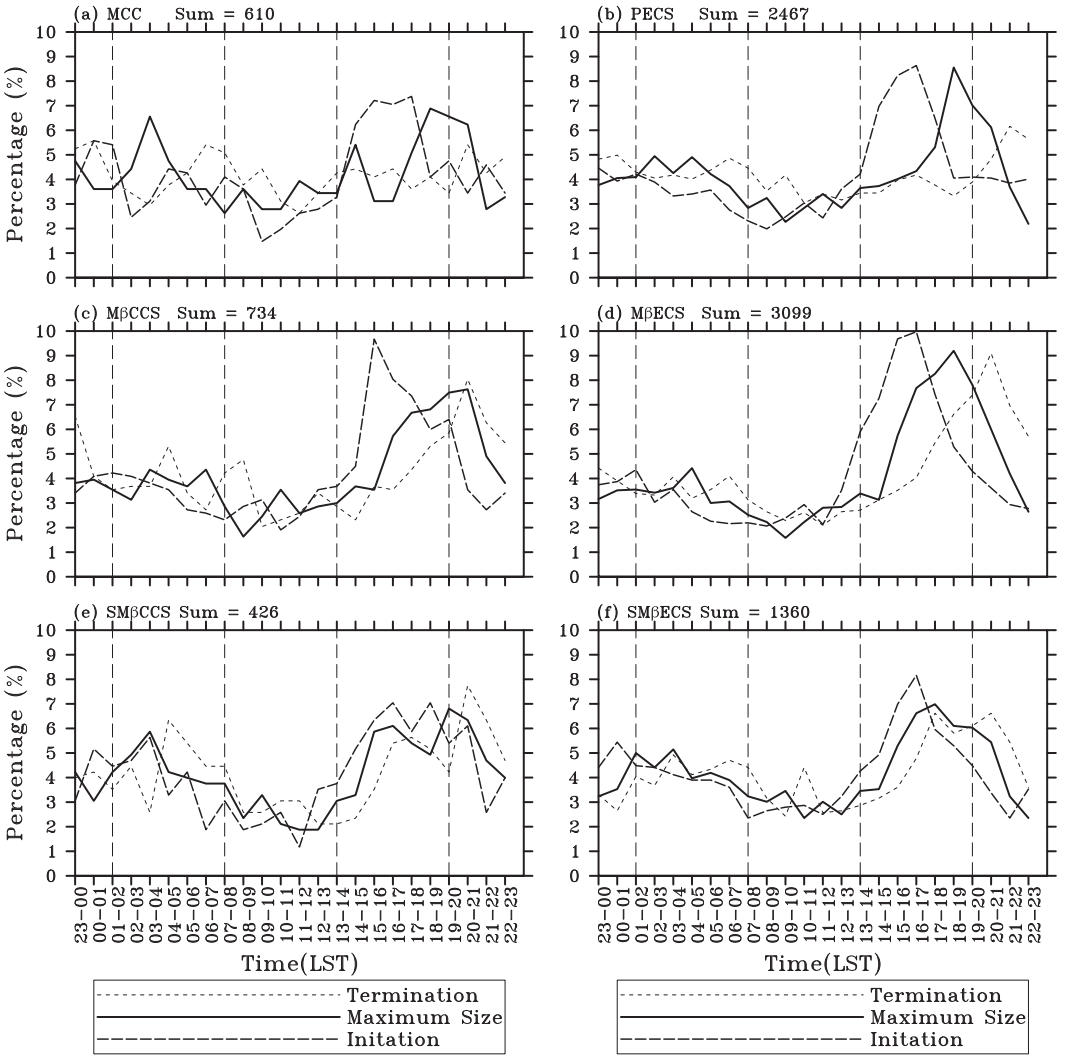

FIG. 9. Frequency for the six types of MCSs during MCS initiation, maturation, and termination stages: (a) MCC, (b) PECS, (c) MβCCS, (d) MβECS, (e) SMβCCS, and (f) SMβECS.

of small-scale systems is about 42 000 km^2. Consistently with the duration criteria discussed before, these large systems persist longer on average (~11 h) than those smaller ones (~4 h) (Table 3).

Although size shows some positive correlation with duration, shape does not appear to have a systematic relationship with the duration of the system. For example, MCCs and PECSs have nearly identical average durations, and MβCCSs and MβECSs also have similar durations (Table 3). Similarly, size does not seem to impact the morphology of the system. It can be observed that the average eccentricities of quasi-circular systems are nearly the same (~0.79; Table 3), and the same is observed for the three types of persisting elongated systems (~0.47; Table 3). Figure 12 shows the eccentricity distribution at the maturation stage. It shows that the distribution of the systems' eccentricity is approximately normal. The peak in eccentricity appears between 0.45 and 0.50, suggesting that most systems are elongated MCSs at the mature stage. Regarding the quasi-circular systems, the peak in eccentricity is between 0.70 and 0.75 and more systems show less circular shape at maturation time.

Another property investigated for each MCS type is the average IR brightness temperature of the cloud shields. The average IR temperatures of the six MCS types are −63.3° (MCC), −62.6° (PECS), −61.3° (MβCCS), −60.6° (MβECS), −61.3° (SMβCCS), and −60.8°C (SMβECS), showing that α-scale (β-scale) systems have an average IR temperature about −63°C (−61°C). The average minimum IR temperatures for the α-scale and β-scale systems are around −83° and −76°C (Table 3), respectively.

TABLE 3. Statistics for each MCS satellite classification: means for each property [China/United States; U.S. data from Jirak et al. (2003)].

Type	Number	Maximum area (10^4 km^2)	Duration (h)			Eccentricity	Temperature (°C)	
			Total	Develop	Decay		Ave	Min
MCC	610/111	16.00/19.33	10.80/10.9	6.14	5.64	0.79/0.83	−63.3	−84.1
PECS	2467/187	18.04/21.35	10.94/10.6	6.14	5.78	0.47/0.50	−62.6	−82.5
MβCCS	734/71	7.40/7.47	6.12/6.1	3.76	3.35	0.79/0.84	−61.3	−77.2
MβECS	3099/96	7.85/8.52	5.91/6.7	3.53	3.36	0.47/0.63	−60.6	−75.7
Above 4 types combined	6910/465	12.16/16.10	8.16/9.2	4.72	4.42	0.54/0.64	−61.6	−79.0
SMβCCS	426	4.23	4.28	2.69	2.57	0.80	−61.3	−75.6
SMβECS	1360	4.26	4.20	2.61	2.59	0.49	−60.8	−75.0
All MCSs	8696	10.53	7.35	4.27	4.03	0.54	−61.5	−78.2

d. *Comparison between Chinese and American MCSs*

This section compares MCSs' characteristics between the United States and China based on the work of Jirak et al. (2003). MCSs forming in both countries extend almost across the same range of latitudes in the Northern Hemisphere and are therefore similarly influenced by extratropical systems and the subtropical jet (Holton 2004). Besides, the steep topographies in the west of both countries play an important role in MCS occurrence and propagation (e.g., Carbone et al. 2002; Xu and Zipser 2011). Thus, comparing MCS characteristics between these two regions can improve our understanding about global variations in these prolific rain-producing systems.

Jirak et al. (2003) includes the following MCS types: MCC, PECS, MβCCS, and MβECS. Thus the comparisons hereafter are based on these four types and the average statistics for the four types are listed in Table 3. The main findings are as follows. First, more systems fall into the larger MCS types (MCC and PECS) than the smaller MCSs (MβCCS and MβECS) in the United States. The MCCs and PECSs account for 64% of the MCSs during 1996–98, and the PECS is the most common type of MCS, accounting for 40% of the total samples. However, a lower proportion of MCCs and PECSs, accounting for only 44% of the MCSs, is found over China and its vicinity. Meanwhile, PECS is the second most common type of MCS, accounting for 35% of the totals.

The second difference is the monthly distribution. The months of May, June, and July have approximately equal probability of MCS occurrence over the United States (Jirak et al. 2003; their Fig. 4). In our study, similar occurrence of systems is observed only in June and July, but not in May. Moreover, the peak in the frequency of the small systems tends to occur in the late season (July), but large systems have maximum frequency in May over the United States. However, both the small and large systems peak in July over China and its vicinity. The occurrence of relatively fewer MCSs in May over China is discussed in section 3b and is mainly attributed to the synoptic conditions that are specific to this region. The third difference is the physical characteristics. It is interesting to note that both the average maximum size and eccentricity of the four MCS types in China are smaller than those in the United States.

Although some MCS characteristics listed above differ between the United States and China, there are also some common features. For example, the elongated systems (PECS and MβECS) in both countries account for the majority of MCSs and have similarly larger average maximum size than the corresponding quasi-circular systems. In addition, the maximum size distribution of the four types exhibits a similar exponential decrease in the number of MCSs when moving toward larger systems. The life span of the same MCS class in both countries is almost the same as well: their average life span is nearly 11 h for the large systems and 6 h for the small ones. Finally, MCSs in the two locations exhibit similar diurnal cycles: the majority of the systems initiate in the late afternoon, reach their maximum extent during the night, and dissipate in the early morning. Besides, although nocturnal MCSs were not explicitly illustrated in Jirak et al. (2003), a secondary peak in the frequency of MCS occurrence during the early morning hours over both nations exists (Fig. 6 in Jirak et al. 2003; Carbone et al. 2002).

4. Summary and discussion

China and its vicinity are commonly affected by heavy rainfall events usually produced from frequent occurrences of MCSs. Over recent decades, many studies have focused on understanding MCSs' features and their physical environments. Using infrared satellite imageries, this study contributes to our knowledge

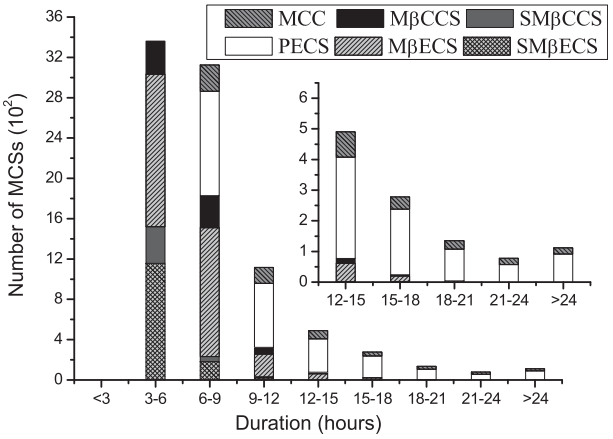

FIG. 10. Bar graph of MCS duration in the warm season (unit: h).

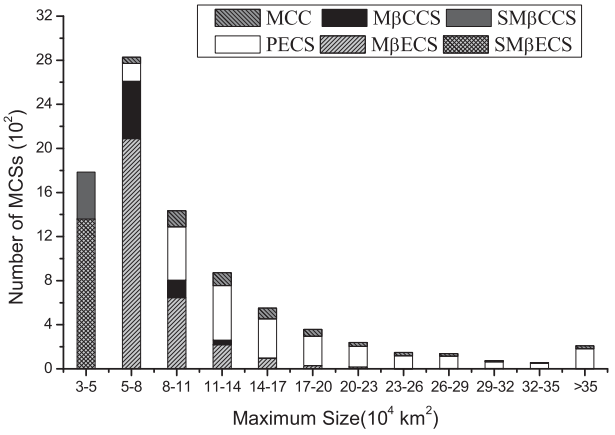

FIG. 11. Area distribution at maturation time (unit: 10^4 km^2).

about MCS activity and morphology by classifying the MCSs into six types: MCC, PECS, MβCCS, MβECS, SMβCCS, and SMβECS. Further analyses of each category are conducted to explore differences in the spatiotemporal and morphological characteristics among the various types.

Based on a hybrid automated-manual method, 8696 MCSs are identified over the studied domain during the warm seasons from 2005 to 2012. More than 80% of all MCSs examined here are elongated systems, and MβECSs are the most dominant type of MCS defined according to their characteristics in infrared images. Spatially, MCSs occur mainly at three zonal bands with latitudes around 20°, 30°, and 50°N. The occurrence frequency of the MCSs is maximized at the zonal band around 20°N and decreases with latitude. Moreover, there are several high-frequency centers in each zonal band.

The monthly frequency shows that MCS occurrence reaches a maximum in July, followed by the months of June and August, with fewer systems observed in May. Moreover, the spatial distribution of MCS occurrence shows that the high-frequency centers shift northward from May to August, and the MCSs over the Tibetan Plateau have an obvious increase in July and August. Besides, regions such as the Bay of Bengal, south of the Himalayas, and the northern Indo-China exhibit a persistent high frequency of MCS occurrence during the warm seasons.

The average life span of the MCSs over China and its vicinity is 7.35 h, approximately 11 h for MCC and PECS, 6 h for MβCCS and MβECS, and 4 h for SMβCCS and SMβECS. The average maximum size of the MCSs is 105 300 km^2 and the peak number of MCSs ranges from 50 000 to 80 000 km^2. Additionally, the shape of the systems has no relevance to the duration and size. That is, the average eccentricity of α-scale elongated (quasi-circular) MCSs is nearly the same as that of β-scale elongated (quasi-circular) systems. The majority of MCSs have eccentricity between 0.45 and 0.49, showing the elongated MCSs account for the majority of MCSs totals. Regarding the diurnal cycle, MCSs generally initiate in the afternoon, mature from dusk to midnight, and dissipate from late evening to dawn. Meanwhile, there is a secondary peak in the frequency of MCS occurrence for the three key stages.

Finally, a comparison between MCSs over China and the United States has been conducted. It is shown that the systems over the Unites States are slightly larger in size and eccentricity than those over China. MCS occurrences over the United States are nearly equal in May, June, and July, whereas MCSs over China occur predominantly in the months of June and July. However, the duration of the same type of MCSs is nearly the same in both countries and the elongated systems dominate the total MCSs both in Jirak et al. (2003) and in this study. Besides, the MCS diurnal cycle in both countries share almost identical diurnal cycles (LST) for the three critical stages.

This study also investigated the spatial distribution of MCSs and identified regions with high concentration of systems. MCSs seem to be organized into zonal bands and there is a clear relationship between the geographic location and the category of MCSs. For example, the majority of the MCSs over the Tibetan Plateau are MβECSs and most MCSs over the Bay of Bengal are α-scale systems. The complex terrain and the characteristics of the underlying surfaces likely play a role for the differences in the distribution of the MCSs. Studies based on *CloudSat*/*CALIPSO* data (Luo et al. 2011) and TRMM precipitation features (Romatschke et al. 2010; Xu 2013) have shown that the horizontal scale, vertical structure, and mixed-phase process of deep convection are largely

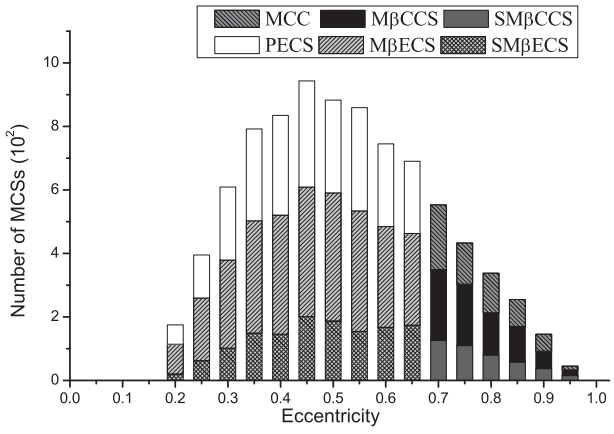

FIG. 12. Eccentricity distribution at maturation stage. The bar width is 0.05 and each bar represents the number of MCSs with eccentricity between the tick mark and tick plus the interval (e.g., the peak number of MCSs shown in the figure is at 0.45, which means these MCSs occur at an eccentricity between 0.45 and 0.50).

different in various underlying surfaces across East Asia. The present study contributes in providing a detailed analysis of the distribution and temporal variability of MCSs that can be useful for future studies addressing the relationships between MCSs and their environments. Subsequent work will focus on the features these various types of MCSs show over the subregions with different underlying surfaces, as well as detailing the synoptic and mesoscale features that are important for the initiation and evolution of these various types of MCSs.

Acknowledgments. We thank the three anonymous reviewers for their helpful comments and suggestions. We acknowledge the National Satellite Meteorological Center of the China Meteorological Administration for providing the satellite data. This work is supported by the National Natural Science Foundation of China Grant 41230421 and the 973 project (2013CB430101) of the Ministry of Science and Technology of China. L. Carvalho acknowledges the National Science Foundation (NSF award AGS 1116105).

REFERENCES

Anderson, C. J., and R. W. Arritt, 1998: Mesoscale convective complexes and persistent elongated convective systems over the United States during 1992 and 1993. *Mon. Wea. Rev.,* **126,** 578–599, doi:10.1175/1520-0493(1998)126<0578:MCCAPE>2.0.CO;2.

Augustine, J. A., and K. W. Howard, 1988: Mesoscale convective complexes over the United States during 1985. *Mon. Wea. Rev.,* **116,** 685–701, doi:10.1175/1520-0493(1988)116<0685:MCCOTU>2.0.CO;2.

——, and ——, 1991: Mesoscale convective complexes over the United States during 1986 and 1987. *Mon. Wea. Rev.,* **119,** 1575–1589, doi:10.1175/1520-0493(1991)119<1575:MCCOTU>2.0.CO;2.

Bartels, D. L., J. M. Skradski, and R. D. Menard, 1984: Mesoscale convective systems: A satellite-data-based climatology. NOAA Tech. Memo. ERL ESG, Vol 8, 58 pp.

Blamey, R. C., and C. J. C. Reason, 2012: Mesoscale convective complexes over southern Africa. *J. Climate,* **25,** 753–766, doi:10.1175/JCLI-D-10-05013.1.

Carbone, R. E., J. D. Tuttle, D. A. Ahijevych, and S. B. Trier, 2002: Inferences of predictability associated with warm season precipitation episodes. *J. Atmos. Sci.,* **59,** 2033–2056, doi:10.1175/1520-0469(2002)059<2033:IOPAWW>2.0.CO;2.

Carvalho, L. M. V., and C. Jones, 2001: A satellite method to identify structural properties of mesoscale convective systems based on the maximum spatial correlation tracking technique (MASCOTTE). *J. Appl. Meteor.,* **40,** 1683–1701, doi:10.1175/1520-0450(2001)040<1683:ASMTIS>2.0.CO;2.

——, ——, and M. A. F. Silva Dias, 2002: Intraseasonal large-scale circulations and mesoscale convective activity in tropical South America during the TRMM-LBA campaign. *J. Geophys. Res.,* **107,** 8042, doi:10.1029/2001JD000745.

Cotton, W. R., M.-S. Lin, R. L. McAnelly, and C. J. Tremback, 1989: A composite model of mesoscale convective complexes. *Mon. Wea. Rev.,* **117,** 765–783, doi:10.1175/1520-0493(1989)117<0765:ACMOMC>2.0.CO;2.

Ding, Y., and J. C.-L. Chan, 2005: The East Asian summer monsoon: An overview. *Meteor. Atmos. Phys.,* **89,** 117–142, doi:10.1007/s00703-005-0125-z.

Durkee, J. D., and T. L. Mote, 2010: A climatology of warm-season mesoscale convective complexes in subtropical South America. *Int. J. Climatol.,* **30,** 418–431, doi:10.1002/joc.1893.

Fei, J. F., R. S. Wu, X. G. Huang, Y. Wang, and X. P. Cheng, 2011: Development of an integrated vertical-slantwise convective parameterization scheme and its associated numerical experiments. *Acta Meteor. Sin.,* **25,** 405–418, doi:10.1007/s13351-011-0402-3.

García-Herrera, R., D. Barriopedro, E. Hernández, D. Paredes, J. F. Correoso, and L. Prieto, 2005a: The 2001 mesoscale convective systems over Iberia and the Balearic Islands. *Meteor. Atmos. Phys.,* **90,** 225–243, doi:10.1007/s00703-005-0114-2.

——, E. Hernández, D. Paredes, D. Barriopedro, J. F. Correoso, and L. Prieto, 2005b: A MASCOTTE-based characterization of MCSs over Spain, 2000–2002. *Atmos. Res.,* **73,** 261–282, doi:10.1016/j.atmosres.2004.11.003.

Ha, Y., Z. Zhong, X. Yang, and Y. Sun, 2013: Different Pacific Ocean warming decaying types and northwest Pacific tropical cyclone activity. *J. Climate,* **26,** 8979–8994, doi:10.1175/JCLI-D-13-00097.1.

——, ——, Y. Sun, W. Lu, 2014: Decadal change of South China Sea tropical cyclone activity in mid-1990s and its possible linkage with intraseasonal variability. *J. Geophys. Res. Atmos.,* **119,** 5331–5344, doi:10.1002/2013JD021286.

Holton, J. R., 2004: *An Introduction to Dynamic Meteorology.* 4th ed. Elsevier, 535 pp.

Houze, R. A., Jr., 1977: Structure and dynamics of a tropical squall-line system. *Mon. Wea. Rev.,* **105,** 1540–1567, doi:10.1175/1520-0493(1977)105<1540:SADOAT>2.0.CO;2.

——, 2004: Mesoscale convective systems. *Rev. Geophys.,* **42,** RG4003, doi:10.1029/2004RG000150.

——, 2007: Monsoon convection in the Himalayan region as seen by the TRMM Precipitation Radar. *Quart. J. Roy. Meteor. Soc.,* **133,** 1389–1411, doi:10.1002/qj.106.

Jiang, J., and M. Fan, 2002: Convective clouds and mesoscale convective systems over the Tibetan Plateau in summer (in Chinese). *Chin. J. Atmos. Sci.,* **26,** 263–270.

Jirak, I. L., W. R. Cotton, and R. L. McAnelly, 2003: Satellite and radar survey of mesoscale convective system development. *Mon. Wea. Rev.,* **131,** 2428–2449, doi:10.1175/1520-0493(2003)131<2428:SARSOM>2.0.CO;2.

Johnson, R. H., S. L. Aves, and P. E. Ciesielski, 2005: Organization of oceanic convection during the onset of the 1998 East Asian summer monsoon. *Mon. Wea. Rev.,* **133,** 131–148, doi:10.1175/MWR-2843.1.

Kane, R. J., C. R. Chelius, and J. M. Fritsch, 1987: Precipitation characteristics of mesoscale convective weather systems. *J. Climate Appl. Meteor.,* **26,** 1345–1357, doi:10.1175/1520-0450(1987)026<1345:PCOMCW>2.0.CO;2.

Laing, A. G., and J. M. Fritsch, 1997: The global population of mesoscale convective complexes. *Quart. J. Roy. Meteor. Soc.,* **123,** 389–405, doi:10.1002/qj.49712353807.

——, and ——, 2000: The large-scale environments of the global populations of mesoscale convective complexes. *Mon. Wea. Rev.,* **128,** 2756–2776, doi:10.1175/1520-0493(2000)128<2756:TLSEOT>2.0.CO;2.

Lau, K.-N., and Coauthors, 2000: A report of the field operations and early results of the South China Sea Monsoon Experiment (SCSMEX). *Bull. Amer. Meteor. Soc.,* **81,** 1261–1270, doi:10.1175/1520-0477(2000)081<1261:AROTFO>2.3.CO;2.

Li, J., B. Wang, and D. Wang, 2012: The characteristics of mesoscale convective systems (MCSs) over East Asia in warm seasons. *Atmos. Oceanic Sci. Lett.,* **5,** 102–107.

Li, Y., Q. Wang, X. Zheng, W. Guo, and W. Wang, 1989: The study of the mesoscale convective complex (MCC) over the southwest and south of China (in Chinese). *Chin. J. Atmos. Sci.,* **13,** 417–422.

Liu, C. T., and E. J. Zipser, 2013: Regional variation of morphology of organized convection in the tropics and subtropics. *J. Geophys. Res. Atmos.,* **118,** 453–466, doi:10.1029/2012JD018409.

Luo, Y., R. Zhang, W. Qian, Z. Luo, and X. Hu, 2011: Intercomparison of deep convection over the Tibetan Plateau–Asian monsoon region and subtropical North America in boreal summer using *CloudSat/CALIPSO* data. *J. Climate,* **24,** 2164–2177, doi:10.1175/2010JCLI4032.1.

Ma, Y., X. Wang, and Z. Tao, 1997: Geographic distribution and life cycle of mesoscale convective system in China and its vicinity (in Chinese). *Prog. Nat. Sci.,* **7,** 701–706.

Ma, Z., J. Fei, X. Huang, and X. Cheng, 2015: Contributions of surface sensible heat fluxes to tropical cyclone. Part I: Evolution of tropical cyclone intensity and structure. *J. Atmos. Sci.,* **72,** 120–140, doi:10.1175/JAS-D-14-0199.1.

Machado, L. A. T., W. B. Rossow, R. L. Guedes, and A. W. Walker, 1998: Life cycle variations of mesoscale convective systems over the Americas. *Mon. Wea. Rev.,* **126,** 1630–1654, doi:10.1175/1520-0493(1998)126<1630:LCVOMC>2.0.CO;2.

Maddox, R. A., 1980: Mesoscale convective complexes. *Bull. Amer. Meteor. Soc.,* **61,** 1374–1387, doi:10.1175/1520-0477(1980)061<1374:MCC>2.0.CO;2.

——, D. M. Rodgers, and K. W. Howard, 1982: Mesoscale convective complexes over the United States during 1981—Annual summary. *Mon. Wea. Rev.,* **110,** 1501–1514, doi:10.1175/1520-0493(1982)110<1501:MCCOTU>2.0.CO;2.

McAnelly, R. L., and W. R. Cotton, 1989: The precipitation life cycle of mesoscale convective complexes. *Mon. Wea. Rev.,* **117,** 784–808, doi:10.1175/1520-0493(1989)117<0784:TPLCOM>2.0.CO;2.

Medina, S., R. A. Houze Jr., A. Kumar, and D. Niyogi, 2010: Summer monsoon convection in the Himalayan region: Terrain and land cover effects. *Quart. J. Roy. Meteor. Soc.,* **136,** 593–616.

Meng, Z., D. Yan, and Y. Zhang, 2013: General features of squall lines in east China. *Mon. Wea. Rev.,* **141,** 1629–1647, doi:10.1175/MWR-D-12-00208.1.

Miller, D., and J. M. Fritsch, 1991: Mesoscale convective complexes in the western Pacific region. *Mon. Wea. Rev.,* **119,** 2978–2992, doi:10.1175/1520-0493(1991)119<2978:MCCITW>2.0.CO;2.

Moncrieff, M. W., and J. S. A. Green, 1972: The propagation and transfer properties of steady convective overturning in shear. *Quart. J. Roy. Meteor. Soc.,* **98,** 336–352, doi:10.1002/qj.49709841607.

Morel, C., and S. Senesi, 2002: A climatology of mesoscale convective systems over Europe using satellite infrared imagery. I: Methodology. *Quart. J. Roy. Meteor. Soc.,* **128,** 1953–1971, doi:10.1256/003590002320603485.

Nesbitt, S. W., and E. J. Zipser, 2003: The diurnal cycle of rainfall and convective intensity according to three years of TRMM measurements. *J. Climate,* **16,** 1456–1475, doi:10.1175/1520-0442-16.10.1456.

Orlanski, L. A., 1975: A rational subdivision of scales for atmospheric process. *Bull. Amer. Meteor. Soc.,* **56,** 527–530.

Parker, M. D., and R. H. Johnson, 2000: Organizational modes of mid-latitude mesoscale convective systems. *Mon. Wea. Rev.,* **128,** 3413–3436, doi:10.1175/1520-0493(2001)129<3413:OMOMMC>2.0.CO;2.

Qie, X., X. Wu, T. Yuan, J. Bian, and D. Lu, 2014: Comprehensive pattern of deep convective systems over the Tibetan Plateau–South Asian monsoon region based on TRMM data. *J. Climate,* **27,** 6612–6626, doi:10.1175/JCLI-D-14-00076.1.

Rodgers, D. M., K. W. Howard, and E. C. Johnston, 1983: Mesoscale convective complexes over the United States during 1982. *Mon. Wea. Rev.,* **111,** 2363–2369, doi:10.1175/1520-0493(1983)111<2363:MCCOTU>2.0.CO;2.

——, M. J. Magnano, and J. H. Arns, 1985: Mesoscale convective complexes over the United States during 1983. *Mon. Wea. Rev.,* **113,** 888–901, doi:10.1175/1520-0493(1985)113<0888:MCCOTU>2.0.CO;2.

Romatschke, U., S. Medina, and R. A. Houze Jr., 2010: Regional, seasonal, and diurnal variations of extreme convection in the South Asian region. *J. Climate,* **23,** 419–439, doi:10.1175/2009JCLI3140.1.

Rotunno, R., J. B. Klemp, and M. L. Weisman, 1988: A theory for strong, long-lived squall lines. *J. Atmos. Sci.,* **45,** 463–485, doi:10.1175/1520-0469(1988)045<0463:ATFSLL>2.0.CO;2.

Tao, Z., H. Wang, and Y. Wang, 1998: A survey of meso-α-scale convective system over China during 1995 (in Chinese). *Acta Meteor. Sin.,* **56,** 166–177.

Velasco, I., and J. M. Fritsch, 1987: Mesoscale convective complexes in the Americas. *J. Geophys. Res.,* **92** (D8), 9591–9613, doi:10.1029/JD092iD08p09591.

Waliser, D. E., and C. Gautier, 1993: A satellite-derived climatology of the ITCZ. *J. Climate,* **6,** 2162–2174, doi:10.1175/1520-0442(1993)006<2162:ASDCOT>2.0.CO;2.

Wang, X., and C. Cui, 2011: A number of advances of the research on heavy rain mesoscale convective systems (in Chinese). *Torrential Rain Disasters,* **30** (2), 97–106.

Wu, X., X. Qie, and T. Yuan, 2013: Regional distribution and diurnal variation of deep convective systems over the Asian monsoon region. *Sci. China Earth Sci.,* **56,** 843–854, doi:10.1007/s11430-012-4551-8.

Xiang, X., and J. Jiang, 1995: Mesoscale convective complexes over the South China mainland (in Chinese). *Quart. J. Appl. Meteor.,* **6,** 9–17.

Xie, B., Q. Zhang, and Y. Wang, 2010: Observed characteristics of hail size in four regions in China during 1980–2005. *J. Climate,* **23,** 4973–4982, doi:10.1175/2010JCLI3600.1.

Xu, W., 2013: Precipitation and convective characteristics of summer deep convection over East Asia observed by TRMM. *Mon. Wea. Rev.,* **141,** 1577–1592, doi:10.1175/MWR-D-12-00177.1.

——, and E. J. Zipser, 2011: Diurnal variations of precipitation, deep convection, and lightning over and east of the eastern Tibetan Plateau. *J. Climate,* **24,** 448–465, doi:10.1175/2010JCLI3719.1.

Yang, B., and Z. Tao, 2005: The analysis of local features of MCC on southeast Tibetan Plateau (in Chinese). *Acta Meteor. Sin.,* **63,** 236–242.

Yu, R., T. Zhou, A. Xiong, Y. Zhu, and J. Li, 2007: Diurnal variations of summer precipitation over contiguous China. *Geophys. Res. Lett.,* **34,** L01704, doi:10.1029/2006GL028129.

Zeng, B., Y. Shen, and T. Xiao, 2013: Statistical analysis of MCS in summer in central-eastern China (in Chinese). *Meteor. Mon.,* **39** (2), 180–185.

Zheng, L. L., J. H. Sun, X. L. Zhang, and C. H. Liu, 2013: Organization modes of mesoscale convective systems over central east China. *Wea. Forecasting,* **28,** 1081–1098, doi:10.1175/WAF-D-12-00088.1.

Zheng, Y., P. Zhu, M. Chen, J. Bai, L. Wang, Y. Li, X. Wei, and Z. Tao, 2004: Meso-α-scale convective systems over Yellow Sea region during summers of 1993–1996 (in Chinese). *Acta Sci. Nat. Univ. Pekinensis,* **40,** 66–72.

——, J. Chen, and P. Zhu, 2008: The characteristic of distribution and spatiotemporal variations of deep convection over China and its vicinity during summer (in Chinese). *Chin. Sci. Bull.,* **53,** 471–481.

Zhuo, H., P. Zhao, C. Li, and Z. Pu, 2012: Analysis of climatic characteristics of mesoscale convective system over the lower reaches of the Yellow River during summer (in Chinese). *Chin. J. Atmos. Sci.,* **36,** 1112–1122.

Zipser, E. J., 1977: Mesoscale and convective-scale downdraughts as distinct components of squall-line circulation. *Mon. Wea. Rev.,* **105,** 1568–1589, doi:10.1175/1520-0493(1977)105<1568:MACDAD>2.0.CO;2.